Supporting Information (SI) Appendix

J. Rajeswari et.al., PNAS

I. LORENTZ MICROGRAPHS

Fig. S1-7 show the full $7.3 \times 7.3\mu m^2$ raw Lorentz micrographs imaged at all magnetic fields investigated in this work.

II. RECIPROCAL-SPACE IMAGES

The full 2D-FTs at four representative magnetic fields $B = 95$ G, 128 G, 160 G and 192 G obtained from the corresponding $7.3 \times 7.3\mu m^2$ micrograph are displayed in Fig. S8. The FTs are obtained from real-space images which have been processed with Gaussian filtering and windowing procedures. Windowing is carried out to remove the frequency-domain effects that appears due to sharp discontinuities at the original image boundaries. These effects can be removed by elementwise multiplication of the original image by a matrix equal to 1 in the center and trending toward 0 at the edges. With this procedure, the intensity of the image decreases towards a value 0 at the image boundaries.

III. SKYRMION POSITIONS AND DELAUNAY TRIANGULATION

To improve the contrast between skyrmions and the background, a Gaussian filter is applied to the original Lorentz images. The position of the skyrmions are then located using an algorithm which finds the centroids of the skyrmions. The procedure is thoroughly checked and manually corrected where needed. We count $\approx$ 9000 skyrmions and estimate the error in locating skyrmions by the algorithm (due to strongly reduced contrast between the skyrmions and the background in some places) to be less than 10. The Delaunay triangulation (DT) of the skyrmion positions is then calculated using the Delaunay function available in the MATLAB® library (Fig. S9-12). The Delaunay triangulated lattice is plotted on top of the real skyrmion lattice to double-check that the defects found by the DT are real.

IV. ANGLE MAP CONSTRUCTION

In the real-space $7.3 \times 7.3\mu m^2$ image, a windowing function is applied to a small region of $0.73 \times 0.73\mu m^2$ and a FT of the image is obtained. We then compute the azimuthal dependence of the intensity of the Bragg peaks determined within a 2π ring that encompasses the Bragg spots. The procedure is repeated by continuously moving the windowed region horizontally as well as vertically to cover the whole $7.3 \times 7.3\mu m^2$ micrograph. In the end, a single Bragg peak is selected and its angle is plotted as a spatial map as shown in the main text Fig. 3 and Fig. S9-12.

V. THICKNESS MAP

After the FIB procedure, we found some tracks of Ga ions running parallel to the surface of the crystal, so called curtaining. This may cause some roughness of the specimen surface. We recorded the thickness map in order to examine any correlation between the spatial distribution of skyrmions and the tracks. No systematic correlation was found. The thickness map was obtained by means of Energy Filtered Imaging on the TEM at 200kV (Fig. S13). Two images, I_0 and I_t, were acquired using elastically scattered electrons and total scattered electrons, respectively. The thickness map was obtained in terms of the relative thickness t/λ via the relation $t/\lambda = \ln(I_t/I_0)$: t is the thickness of the specimen and λ is the mean free path of the total inelastic scattering [1]. The map was measured at room temperature. The thickest part of the specimen was measured to be 150 nm with scattering electron microscopy.

VI. BRIEF DESCRIPTION OF SUPPLEMENTARY MOVIE

Supplementary Movie1: TimeSequence.avi. Whole sequence of the skyrmion images shown in Fig. 4 of the main text as function of time from 0 s to 50 s with an interval of 0.5 s.

[1] Egerton, R. F. *Electron energy-loss spectroscopy in the electron microscope.* New York: Plenum Press, 2nd edition, (1996).

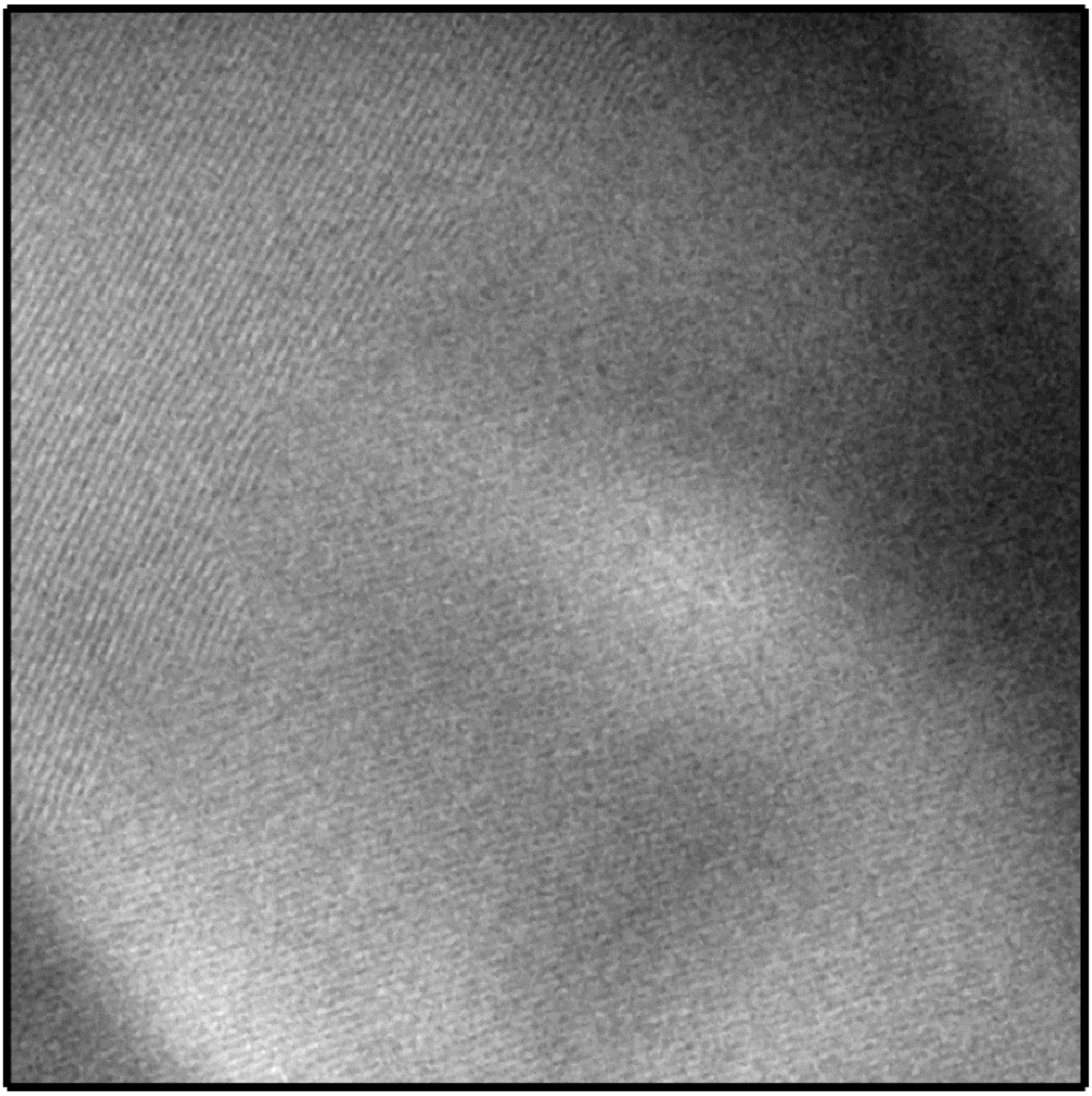

FIG. S1. $7.3 \times 7.3 \mu\mathrm{m}^2$ real-space image of the helimagnetic phase at $B = 95$ G.

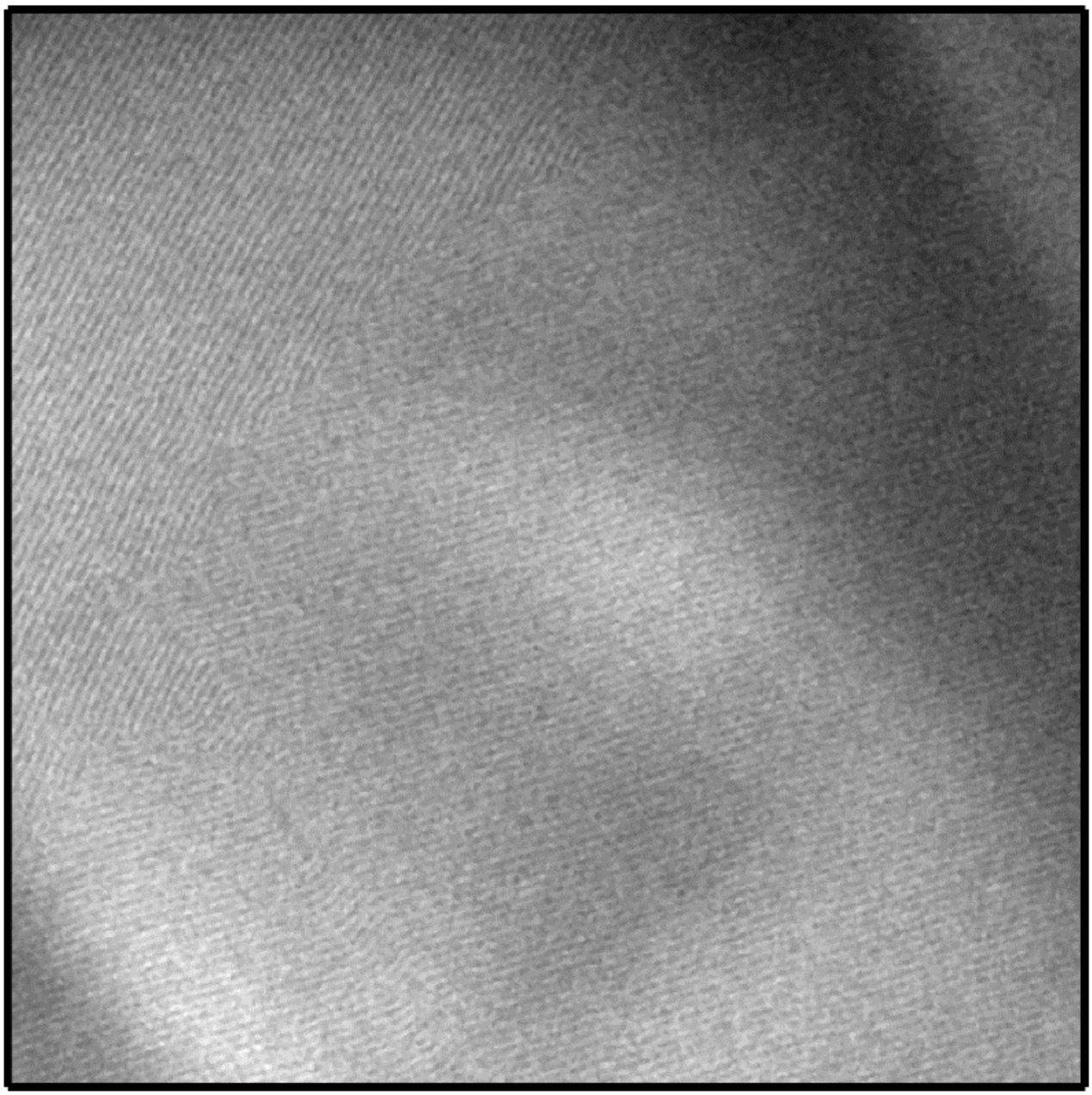

FIG. S2. $7.3 \times 7.3 \mu\mathrm{m}^2$ real-space image of the helimagnetic phase at $B = 128$ G.

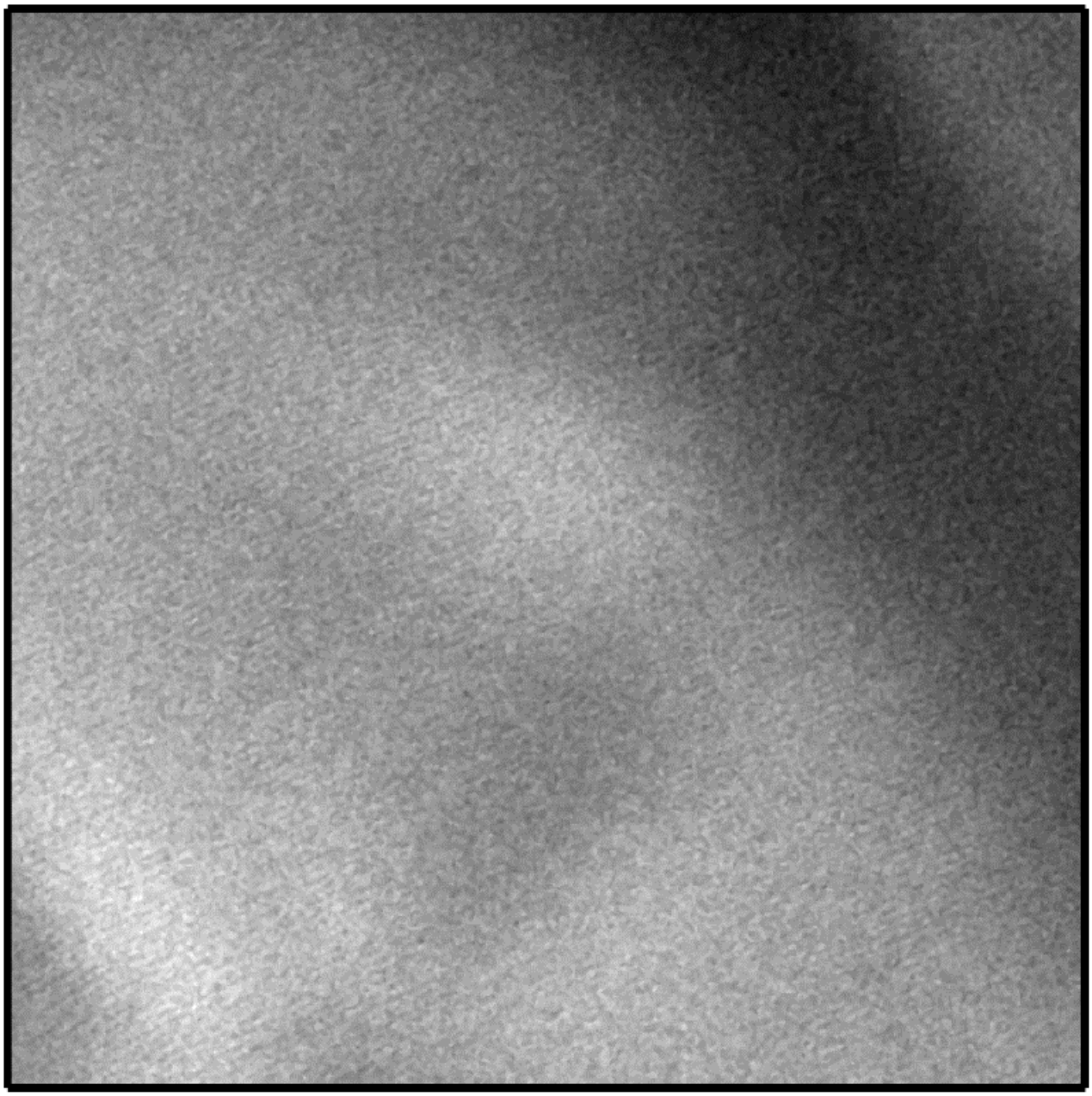

FIG. S3. $7.3 \times 7.3 \mu\mathrm{m}^2$ real-space image of the glassy phase at $B = 160$ G.

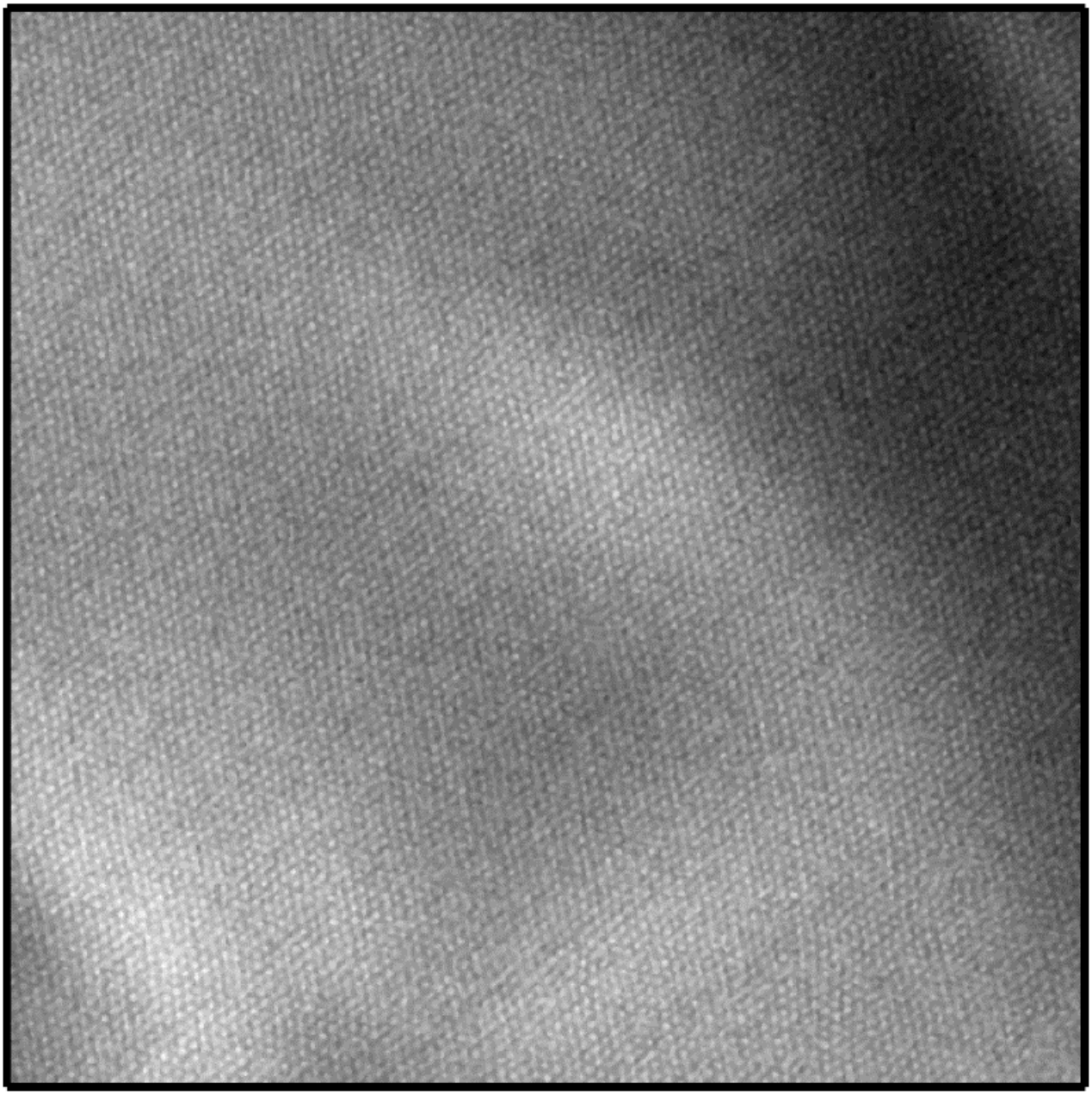

FIG. S4. $7.3 \times 7.3 \mu\mathrm{m}^2$ real-space image of the skyrmion phase at $B = 192$ G.

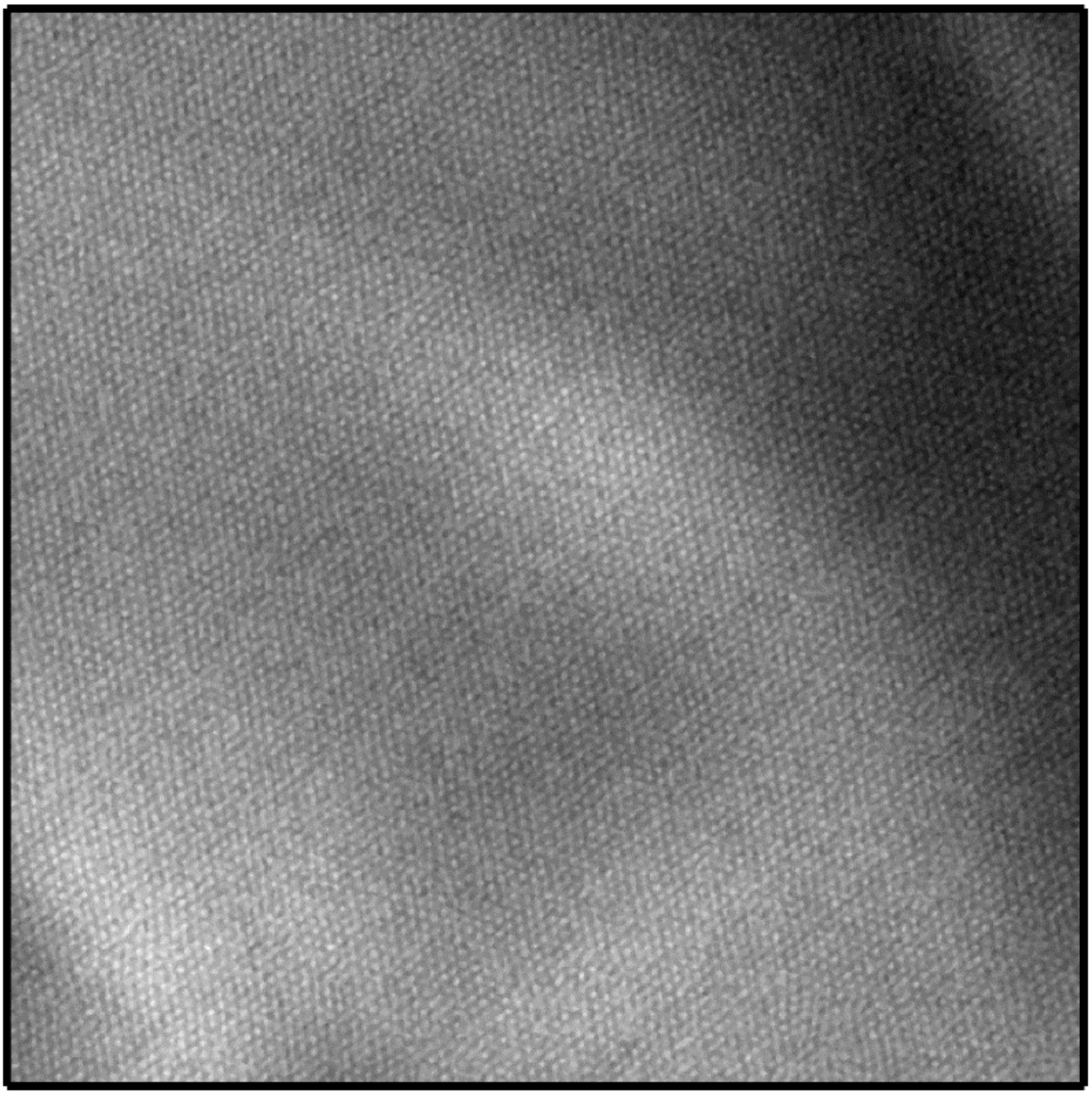

FIG. S5. $7.3 \times 7.3 \mu\mathrm{m}^2$ real-space image of the skyrmion phase at $B = 225$ G.

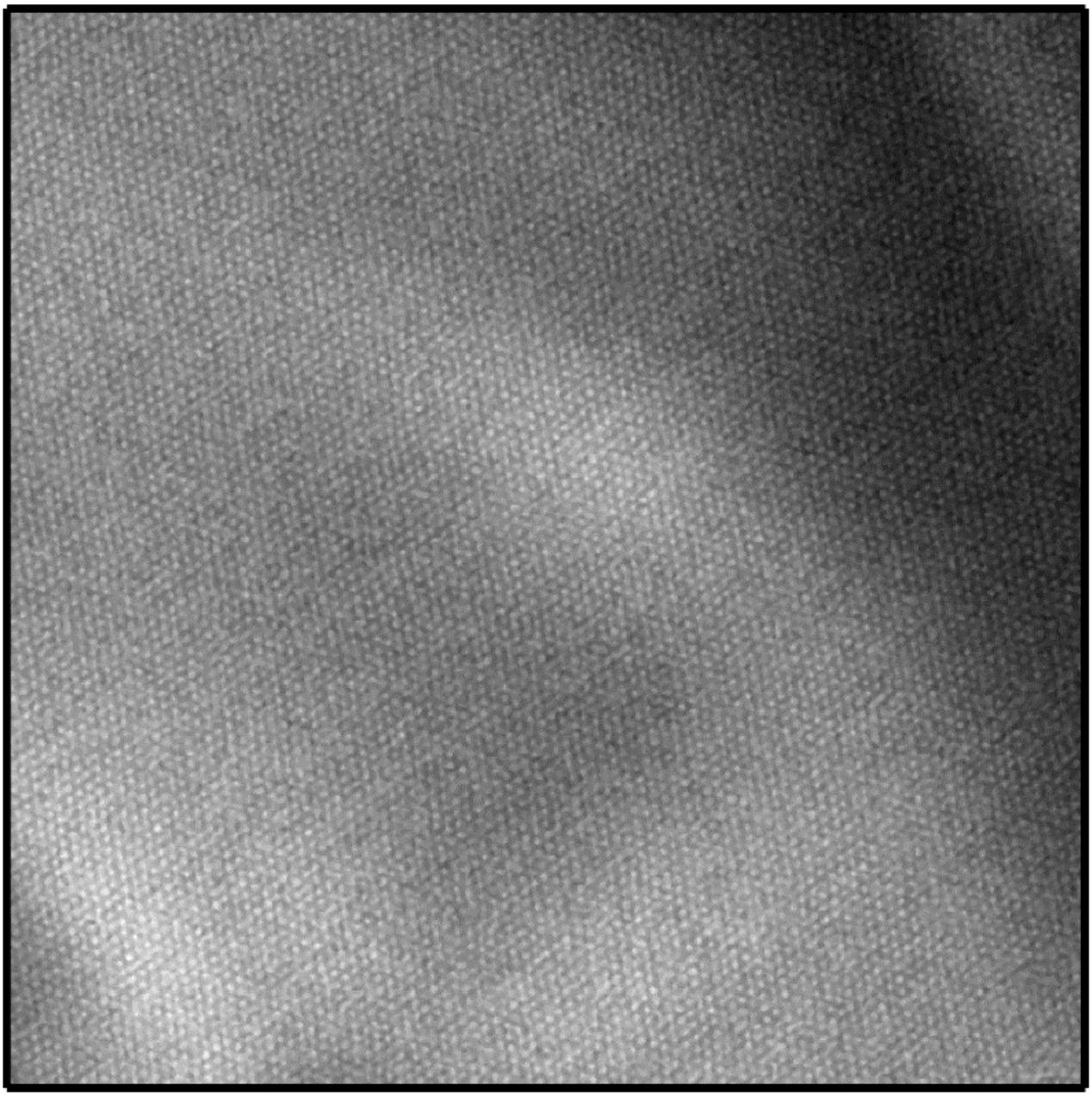

FIG. S6. $7.3 \times 7.3 \mu\mathrm{m}^2$ real-space image of the skyrmion phase at $B = 354$ G.

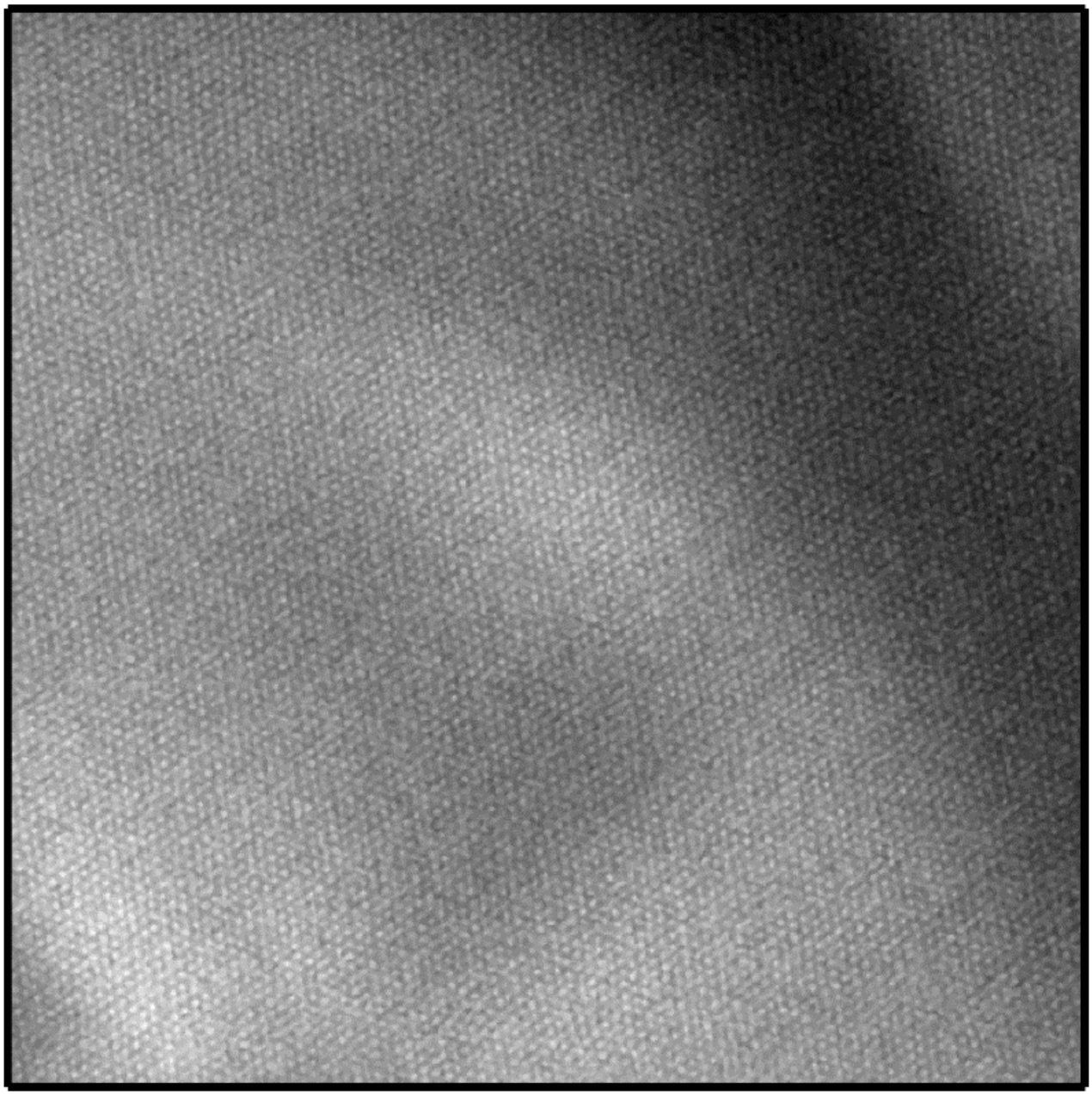

FIG. S7. $7.3 \times 7.3 \mu\mathrm{m}^2$ real-space image of the skyrmion phase at $B = 483$ G.

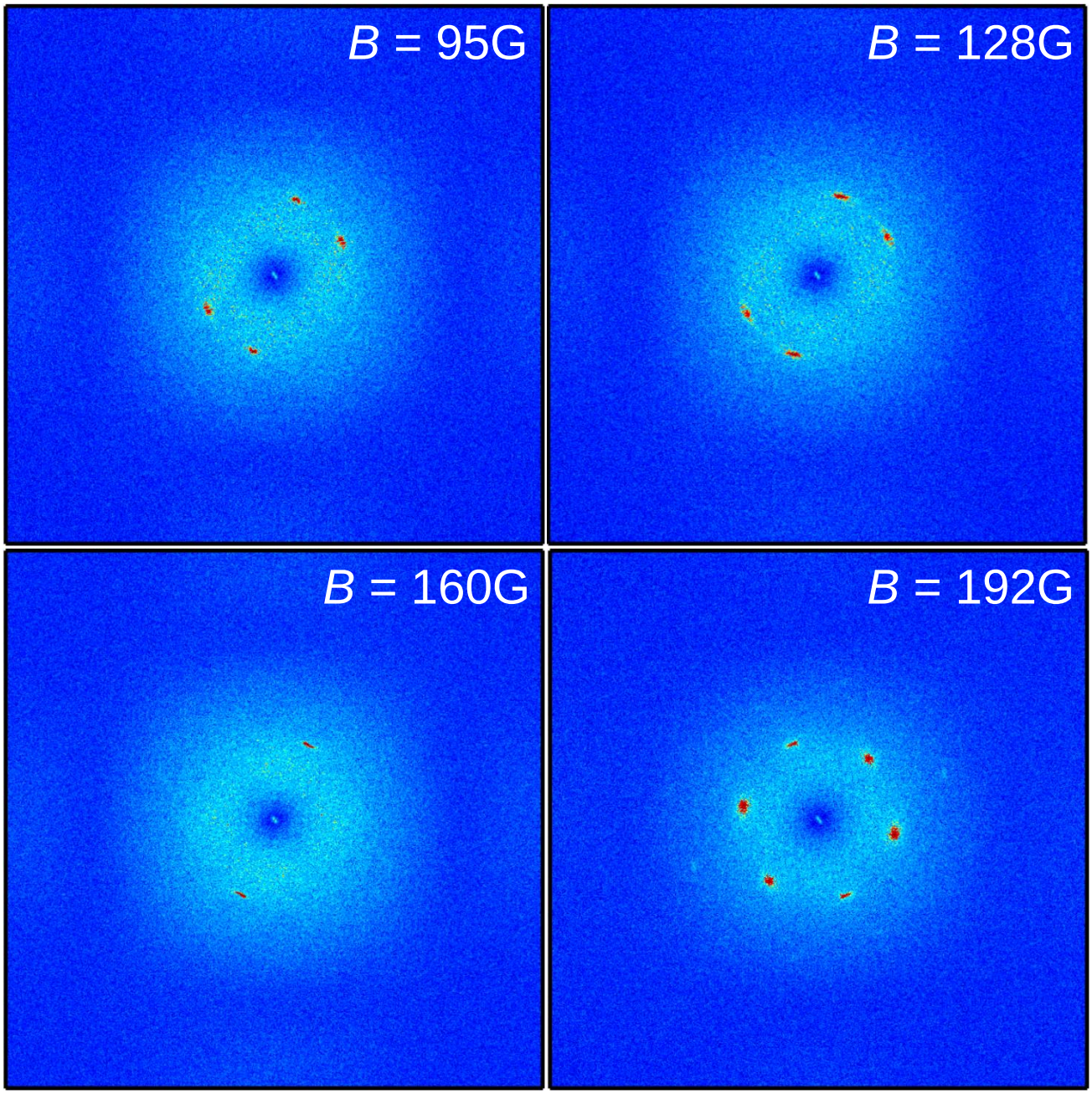

FIG. S8. The full 2D-FT's at four magnetic fields $B = 95$ G, 128 G, 160 G and 192 G obtained from the corresponding whole real-space image.

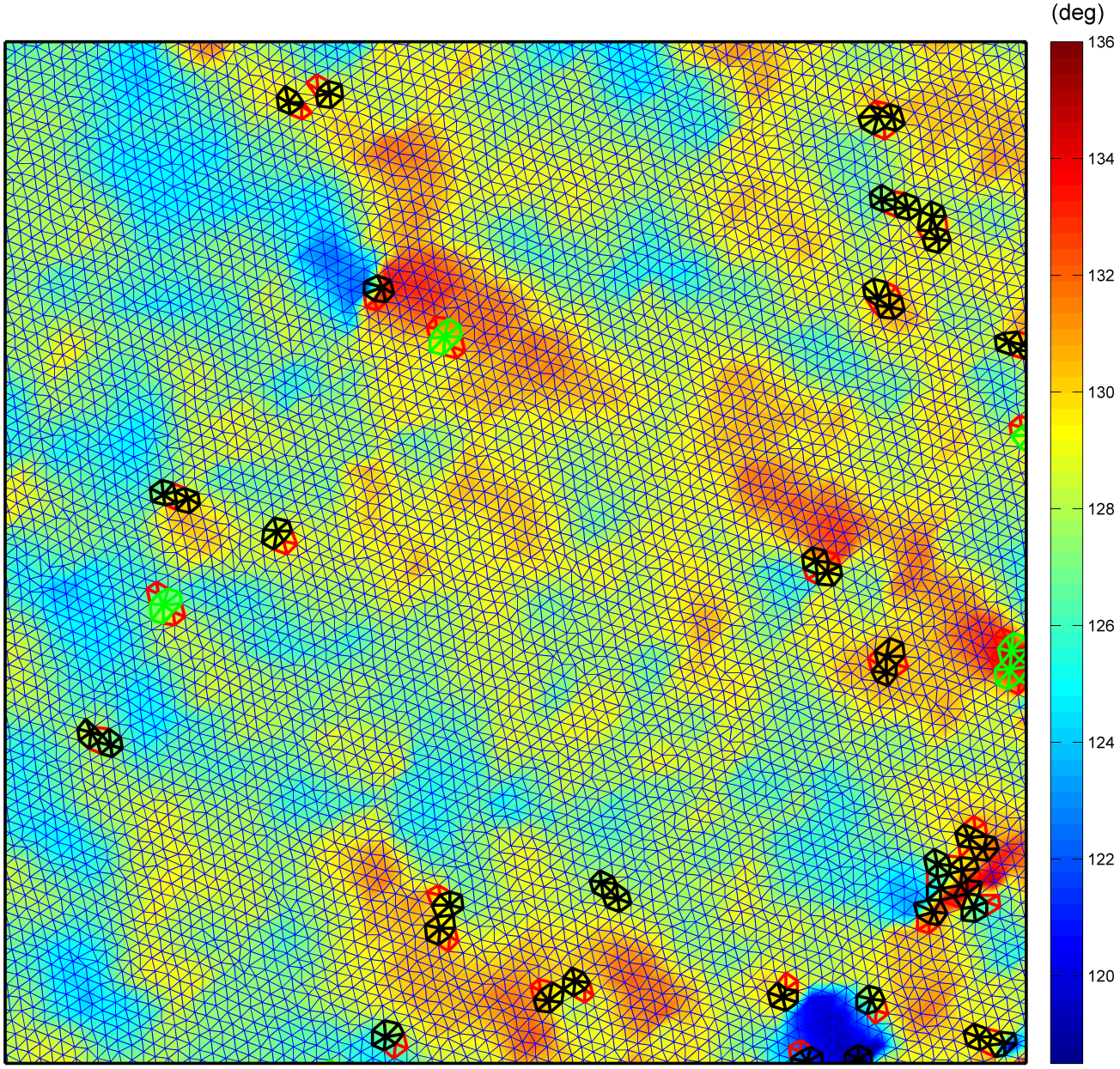

FIG. S9. Angle map of the skyrmion lattice at $B = 192$ G computed for the whole $7.3 \times 7.3 \mu\text{m}^2$ micrograph plotted together with the Delaunay triangulation and defects.

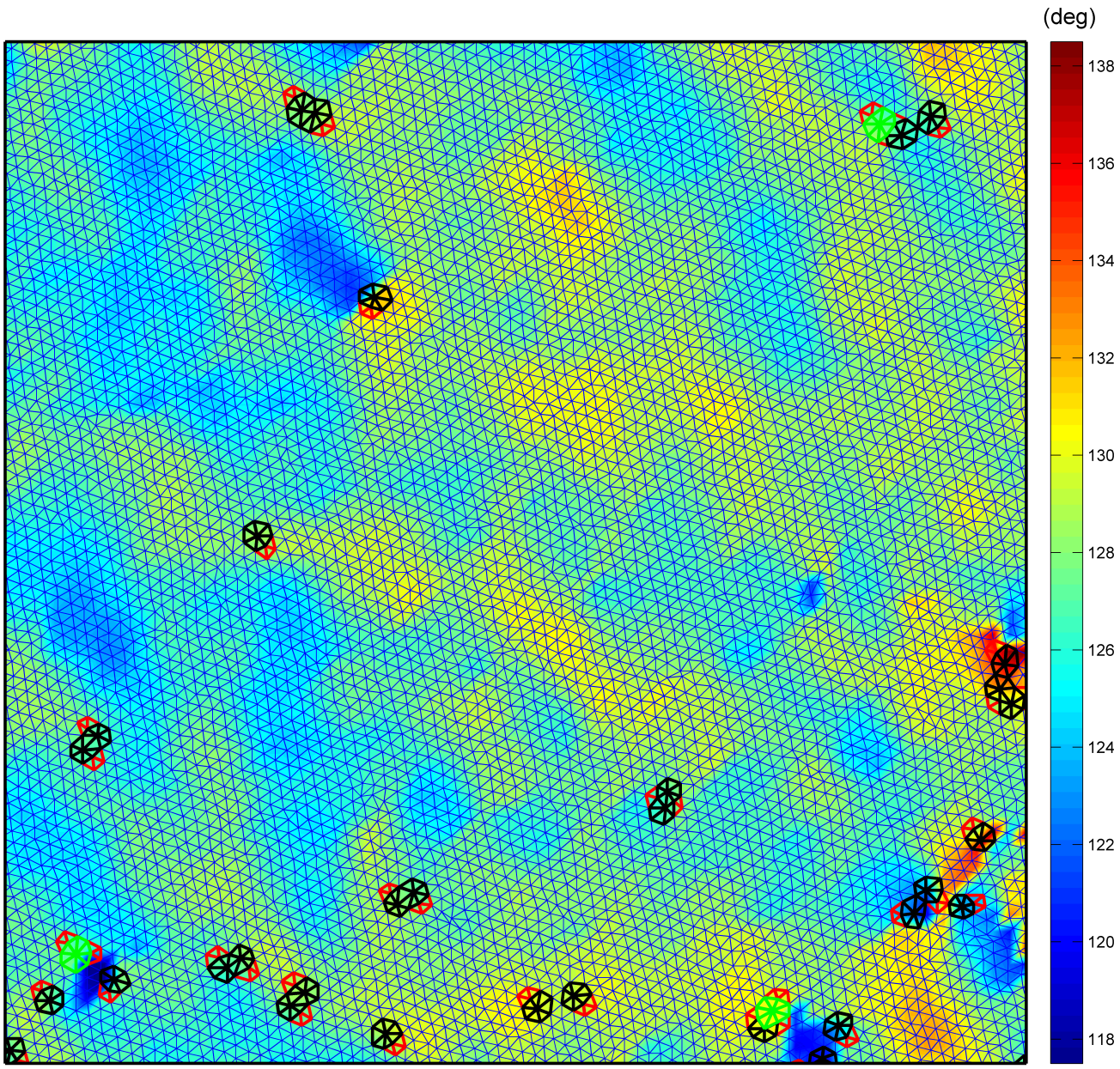

FIG. S10. Angle map of the skyrmion lattice at $B = 225$ G computed for the whole $7.3 \times 7.3 \mu\text{m}^2$ micrograph plotted together with the Delaunay triangulation and defects.

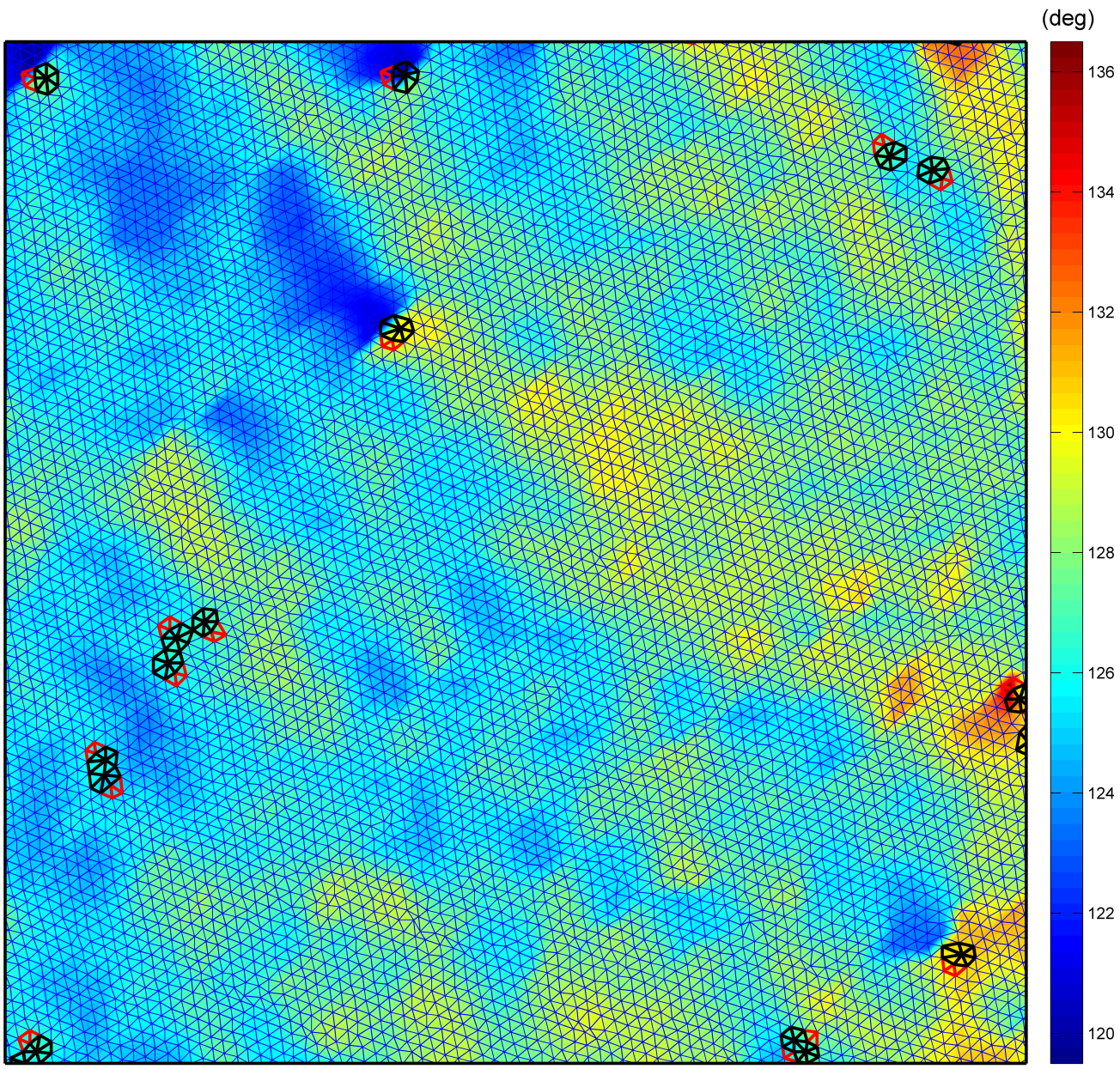

FIG. S11. Angle map of the skyrmion lattice at $B = 354$ G computed for the whole $7.3 \times 7.3 \mu\text{m}^2$ micrograph plotted together with the Delaunay triangulation and defects.

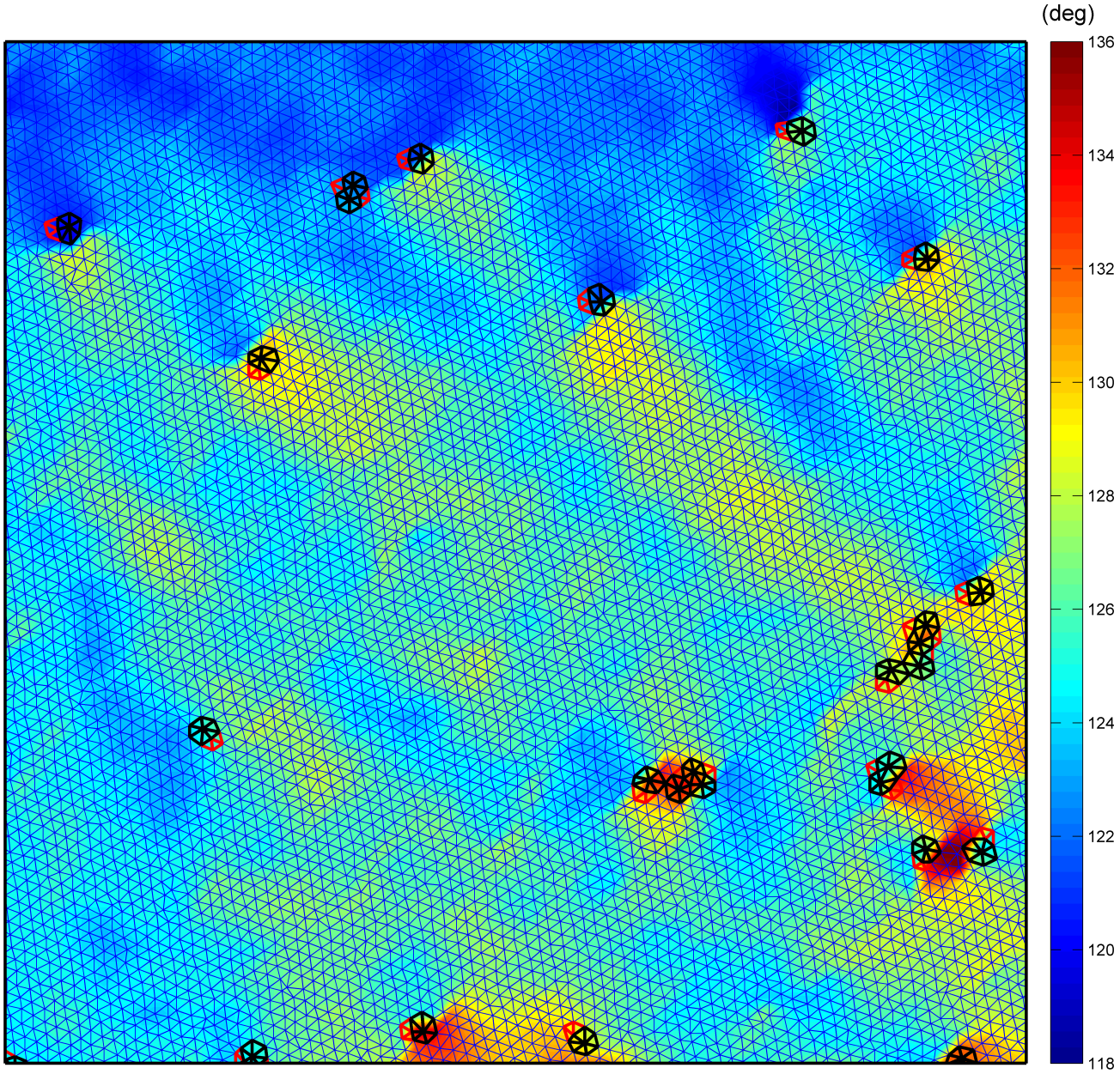

FIG. S12. Angle map of the skyrmion lattice at $B = 483$ G computed for the whole $7.3 \times 7.3 \mu\text{m}^2$ micrograph plotted together with the Delaunay triangulation and defects.

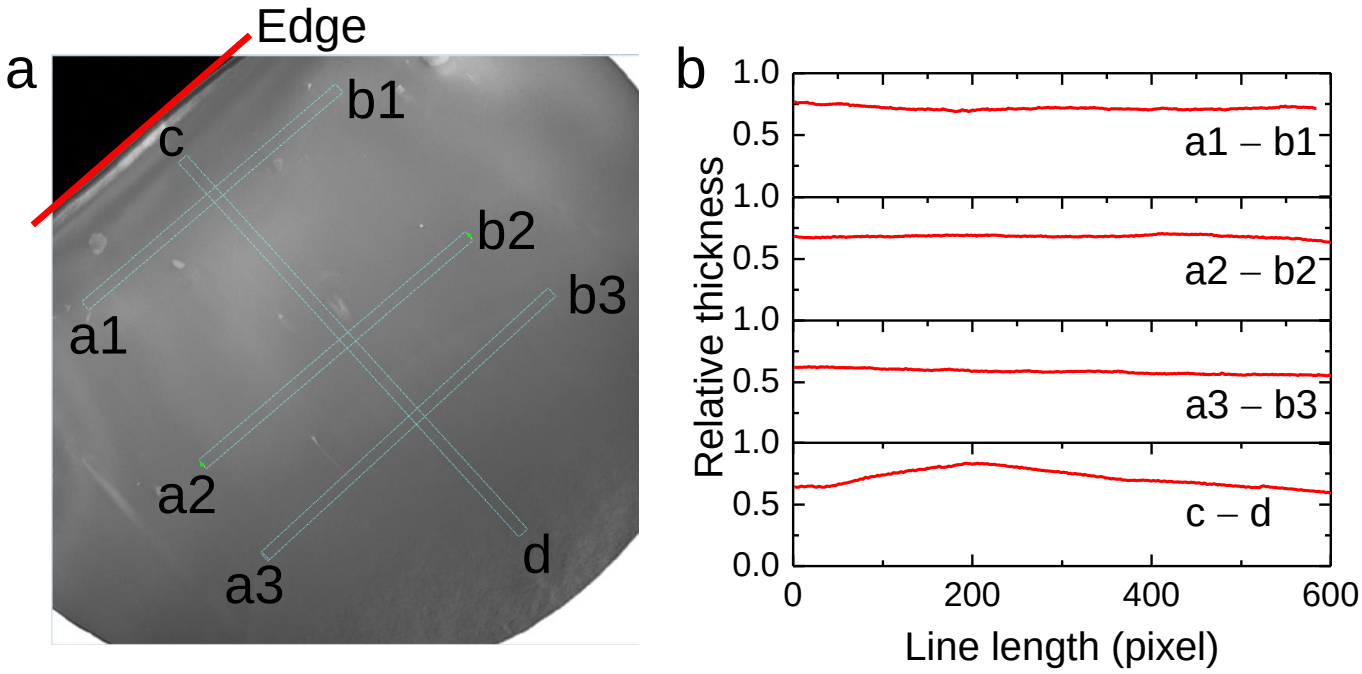

FIG. S13. **(a)** $7.3 \times 7.3 \mu m^2$ thickness map of our sample. Four lines each of 20 pixels thick are marked in the thickness map along which line profiles were recorded. The line profiles are shown in **(b)**. The relative thickness remains practically constant at 0.6 along the lines parallel to the edge whereas for line perpendicular to the edge, the relative thickness varies between $0.6 - 0.7$.